Laboratori Nazionali di Frascati

LNF-93/018 (IR)
30 Aprile 1993

B. Babusci, S. Bianco, R. Casaccia, L. Daniello, F.L. Fabbri, M. Giadoni, M. Lindozzi, L. Passamonti, V. Russo, S. Sarwar, L. Votano, A. Zallo, L.E. Casano, A. D'Angelo, D. Moricciani, F. Ghio, B. Girolami, D. Hertzog, S. Hughes, P. Reimer, R. Tayloe:

TEST OF PB/SCIFI ELECTROMAGNETIC CALORIMETER PROTOTYPES WITH LOW ENERGY PHOTONS AT LADON

PACS.: 29.40.Vj

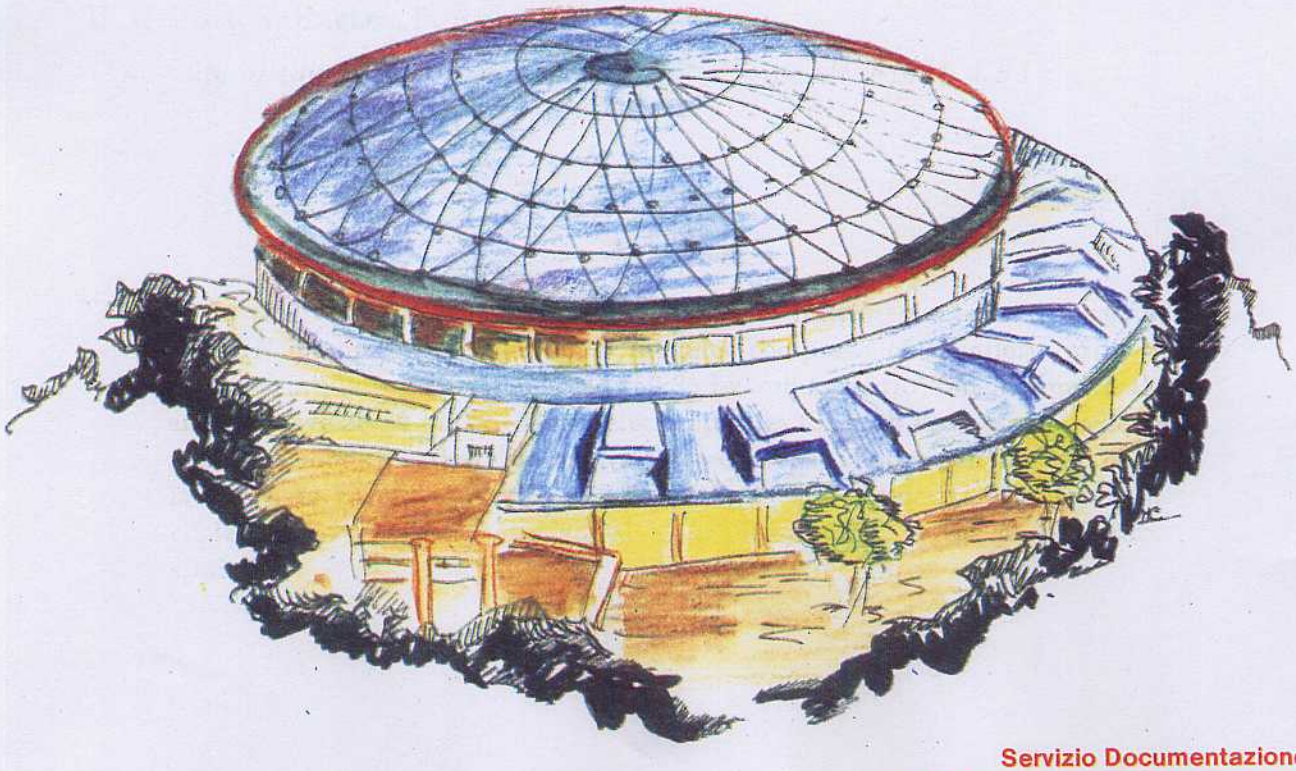

Servizio Documentazione
dei Laboratori Nazionali di Frascati
P.O. Box, 13 - 00044 Frascati (Italy)

INFN - Laboratori Nazionali di Frascati
Servizio Documentazione

LNF-93/018 (IR)
30 Aprile 1993

TEST OF PB/SCIFI ELECTROMAGNETIC CALORIMETER PROTOTYPES WITH LOW ENERGY PHOTONS AT LADON

D. Babusci, S. Bianco, R. Casaccia, L. Daniello, F.L. Fabbri, M. Giardoni, M. Lindozzi, L. Passamonti, V. Russo, S. Sarwar, L. Votano, A. Zallo

INFN - Laboratori Nazionali di Frascati, V. E.Fermi 40, I-00044 Frascati, Italy

L.E. Casano, M. Capogni, A. D'Angelo, D. Moricciani

INFN, Sezione Roma II, V. della Ricerca Scientifica 1, I-00173 Roma, Italy

F. Ghio, B. Girolami

Istituto Superiore di Sanitá and INFN, Sezione Sanitá, V.Regina Elena 299, I-00161 Roma, Italy

D. Hertzog, S. Hughes, P. Reimer, R. Tayloe

University of Illinois at Urbana-Champaign, Urbana, IL 61801, USA

Abstract

In this work we report the complete set of measurements carried out at LADON on small size calorimeter modules composed of a uniform array of plastic scintillating fibers and lead (50:35 by volume ratio) for photons in the energy range 20-80 MeV. Calorimeter properties for both head-on and side-on incidence conditions have been investigated. With photons hitting the fibers laterally, an energy resolution of $4.8\%/\sqrt{E[GeV]}$ is obtained. This figure includes a $2\%/\sqrt{E[GeV]}$ term added in quadrature due to the photoelectron statistics.

1 Introduction

A lot of interest has been focussed in the last few years on new methods of measuring low-energy photons with good energy and spatial resolution in large detection volumes. Calorimeters employing crystals or noble liquid gases provide excellent resolutions, but are costly. Moreover, liquid gas calorimeters require complex cryogenic techniques and do not guarantee real hermeticity. Alternative techniques should conjugate excellent performance (good energy and spatial resolution, fast timing, hermeticity) with reasonable cost, easy prototyping and modular construction. Experiments at LEAR [1] and CEBAF [2] have achieved outstanding results in the development of noncompensating lead/scintillating fiber (Pb/SCIFI) calorimeters able to reach resolutions between $6\%/\sqrt{E[GeV]}$ and $9\%/\sqrt{E[GeV]}$ in the 35MeV-5GeV energy range.

Various techniques have been developed to construct lead-embedded fiber calorimeters, including high-density lead alloys with low melting point [3], perforated lead volumes with holes to position the fibers [4], and grooved lead foils stacked with fibers [1]. The last technique has permitted, using 1-mm-diameter fibers, a very homogeneous 50:35 fiber-to-lead ratio, which represents a limit mechanically difficult to increase. The published results show how these detectors achieve $6 - 9\%/\sqrt{E[GeV]}$ energy resolutions in the energy range 35 MeV-5 GeV [1, 5]. The same technique has been selected for electromagnetic (em) calorimetry for KLOE experiment [6] at the $DA\Phi NE$ ϕ-factory [7].

This study reports a set of detailed measurements aimed to characterize performances and limitations of lead/scintillating fiber detectors in the ultra-low (down to 20 MeV) photon energy region. Three $\sim 10 \times 10 \times 22$ cm^3 prototypes, built with the same technique, have had their performances tested over a wide range of angular conditions with $20 - 80 MeV$ photons. The energy resolution of the modules in good geometry conditions is $4.8\%/\sqrt{E[GeV]}$, which includes a term of $2\%/\sqrt{E[GeV]}$ added in quadrature due to photoelectron statistics.

2 Assembly of the Prototypes

Three prototype modules have been studied. Module A was built at the University of Illinois at Urbana-Champaign [1]; modules B and C, at INFN Frascati National Laboratory. All three detectors are made of grooved lead(+6% Sb) foils [8] and 1-mm-diameter scintillating fibers (fig.1).

A description of the construction of the grooved lead plates and assembling technique for module A is reported in detail elsewhere [1]. To assemble modules B and C, the fibers were cut to size and then placed in a transport frame to permit their positioning in the grooves during the procedure of stacking and gluing them, alternately with the lead foils. Once assembled, the fibers form a periodical triangular lattice, with an interaxial distance of 1.35 mm between the nearest fibers.

Module A uses Optectron [9] S101-S 1-mm-diameter scintillating fibers and Bicron

[10] BC600 optical cement; module B, Optectron S101-S 1-mm scintillating fibers and NE581 optical cement[11]; module C, Pol.Hi.Tech 0042 1-mm scintillating fibers [12] and BC600 glue. All the modules had the same external dimensions ($9.8 \times 9.8 \times 22\, cm^3$) after machining and polishing the two faces lying orthogonal to the fibers. The assembled modules have a density which may vary within $\sim 7\%$, depending on the assembly procedures followed (amount of glue, pressure applied). The densities of modules A and B were measured and found to be $4.58 \pm 0.02\ g/cm^3$ and $4.63 \pm 0.02\ g/cm^3$ respectively, corresponding to a $\sim$ (15 : 50 : 35) volume ratio between glue, fiber and Pb/Sb alloy. The radiation length X_o and Molière radius R_M are evaluated from the material composition via the relationships [13]:

$$\frac{1}{X_o} = \sum_i \frac{f_i}{(X_o)_i} \qquad \frac{1}{R_M} = \frac{1}{E_s} \sum_i \frac{f_i (E_c)_i}{(X_o)_i}$$

where for each i^{th} medium, f_i is the volume fraction, $E_s = \sqrt{4\pi/\alpha}\, m_e c^2 = 21.2\ MeV$, and E_c is the critical energy. The computed values are $X_o = 1.61\ cm, R_M = 3.5\ cm$, with each module corresponding to a total depth of $14\, X_o$. However, the concept of 'radiation length' relates correctly to the high-energy domain only. In the energy range studied, Montecarlo simulation showed that the composite material employed will exhibit a fraction of the photon energy left at a depth $t[cm]$, according to the parametrization $\approx \exp(-t/6.2)$. Therefore, the prototypes have about 97% of the initial photon energy deposited in their thickness (22 cm). The radius of the cylindric volume containing 90% of the shower energy is 2.9 cm.

Aluminized mylar tape covers the entrance face of each module, while the rear (readout) face is coupled to an acrylic lightguide via a 1-cm air gap. The lightguide (tapered from square to circular cross-section) funnels the light from the fibers to a 10-dynode 9902KB EMI [14] photomultiplier (PMT) with a 32-mm diameter photocathode, whose typical quantum efficiency is 20% at 420 nm. The PMT is glued to the exit face of the lightguide. The lightguide is enclosed in aluminum foil and both lightguide and module are wrapped in black tape. The geometrical ratio of the entrance area (a) to the exit area (a') of the lightguide used is about 12. The maximum geometrical ratio allowed in an ideal concentrator, i.e., the ratio permitting all the rays entering the lightguide to emerge at the exit face, is determined by the generalized étendue [15]:

$$\left(\frac{a}{a'}\right)_{max} = \left(\frac{n_{a'} \sin\theta_{a'}}{n_a \sin\theta_a}\right)^2$$

where $\theta_a, \theta_{a'}$ are, respectively, the half angle of the input light cone and the largest angle of the emergent ray. In the case of scintillating fibers coupled in air to an acrylic lightguide with adiabatic reduction in cross-section,

$$\theta_a = \arcsin\left[n_{core} \sin\left(\arccos\frac{n_{clad}}{n_{core}}\right)\right],$$

while $\theta_{a'}$ is related to the critical angle for a light ray channeled inside the lightguide:

$$\theta_{a'} = 90^o - \theta_c.$$

Because of the difference of the refraction indices of the Optectron and Pol.Hi.Tech (see tab.1), $\theta_a = 27^o$ for modules A and B; $\theta_a = 22^o$, for module C. Ideally, to permit full light-channeling efficiency, the areal reduction factor of the adiabatic lightguide should not be greater than

$$\left(\frac{a}{a'}\right)_{max} = \frac{n^2_{lightguide} - 1}{n^2_{core} - n^2_{clad}} = 2.3$$

in the first case, and

$$\left(\frac{a}{a'}\right)_{max} = 4.0$$

in the second case.

In the adiabatic approximation, lightguides having an areal reduction factor of 12, as those used here, would account for efficiencies

$$\frac{\left(\frac{a}{a'}\right)_{max}}{\frac{a}{a'}}$$

of about 19% and 33%, respectively. Additional inefficiency (35 – 40%) arises from window losses at the PMT-lightguide interface as well as at the fiber-lightguide gap, and from absorption and reflectivity losses at the acrylic-air interface of the lightguide.

The photomultipliers coupled to the three modules were selected with the requirement that they had similar photocathodic sensitivity. Each photomultiplier-ADC[16] system was calibrated in photoelectron units by flashing the photocathode with light-emitting diodes and using a coarse approximation:

$$N_{pe} = \frac{1}{\sigma^2_{ADC}} \qquad (1)$$

where σ_{ADC} is the relative rms width of the pulse height distribution at the anode. Dynode gain fluctuations and nonuniformities [17] introduce a systematic error of 10 $\sim$ 15 % in this estimate.

To select equal-sensitivity PMTs, each one of them was coupled via a hexagonal lightguide, which acts as a light mixer and guarantees a uniform illumination of the photocathode, to a scintillator counter irradiated by an α source. The lightguide was glued to the scintillator counter, while for good reproducibility, the coupling at the PMT face was effected in air by means of a ferrule positioning system. The accuracy over several positionings was measured and found better than 3%. The batch of tested PMTs showed photocathode sensitivities ranging over a factor of $\sim$ 1.5. The criteria for selecting the three PMTs were, that they be close to the distribution mean and have sensitivity within the accuracy of eq.1 and the coupling reproducibility. For experimental ease, the photoelectron scales of the three selected PMT-ADC systems were renormalized to provide equal nominal sensitivities.

All the modules were tested with cosmic ray muons, while modules A and B were also exposed to a 20-80 MeV photon beam. The tests with photons were performed

with the modules in both side-on (photon entering the module approximately perpendicular to the fiber axis) and head-on (photon entering the module approximately parallel to the fiber axis) configurations. The two configurations can be regarded as extreme cases for understanding the behaviour of the detector under various photon incidence angles.

3 Test with Cosmic Muons

A three-counter telescope selected cosmic rays simultaneously crossing the 10-cm-thick detector perpendicular to the lead foils, as well as a 30-cm-thick Pb absorber (muon momentum $\geq$ 450 MeV/c). On the entrance face, the telescope defined a 3×3 cm^2 spot. The typical distribution of visible energy released in the detector is shown in fig.2. The lead thickness was varied from 20 cm to 40 cm to verify that the most probable value of the distribution remained unchanged, so that it could be accepted as an easy-to-reproduce calibration signal.

The most probable value of the visible energy deposited by the muons is shown in fig.3 as a function of the distance from the face of the module coupled to the lightguide. The light attenuation behaviour observed with cosmic muons well reflects the characteristics of light transport along the fibers.

The light collected at the end of a scintillating fiber is composed of two components: the light channeled by total internal reflection at the core-cladding interface and the light trapped at the cladding outer surface. While the light trapped in the core exhibits a reasonable attenuation length (typically 50 cm or more in the initial meter), the component trapped at the cladding-air interface exhibits an attenuation length one order of magnitude shorter, due to the unpredictable quality of the fiber surface. When tested in an air environment with a collimated β source [18], the light in the Optectron S101-S SCIFI is attenuated, as shown in fig.3b, where the contribution of the cladding light has been eliminated. The fibers assembled in the modules are encapsulated within the optical cement, which has refraction index ($n = 1.56$) similar to that of the core: therefore, the cladding light no longer experiences total internal reflection and escapes at the cladding-glue interface. This is well illustrated by fig.3b, where the fibers already assembled in the prototype show an attenuation curve very similar to the one measured before the assembly for the light trapped in the core.

The light yield from cosmic muons per crossed cm of detector, at 10 cm from the readout face, corresponds to (21.1 ± 0.5) pe/cm for module A, (23.0 ± 0.5) pe/cm for module B, and (15 ± 1) pe/cm for module C. These figures include trapping efficiency and attenuation within the fiber, losses due to the coupling of various media, lightguide efficiency and, finally, the PMT quantum efficiency. Due to the equality of the PMT-ADC nominal sensitivity and to the absolute calibration of the photoelectron scale, the close agreement between modules A and B reflects the homogeneity of the fibers, the precision of the mechanical couplings and the control of the optical-coupling efficiency; while in module C, the improved lightguide efficiency is offset by the reduced trapping efficiency and the lower scintillation [19] of the fibers employed.

4 Tests with Photon Beam

The LADON tagged photon beam [20] is produced via inverse-Compton scattering of light from an Ar laser off the ADONE storage ring electrons. The end-point of the photon energy spectrum can be varied from 20 to 80 MeV by adjusting the energy of the ADONE electrons. Both the photon-beam spot and the shape of the energy spectrum depend on the collimation selected. A microstrip silicon detector tags the photon energy by measuring the momentum of the scattered ADONE electron. The tagging system is calibrated after each change in the photon-beam setup using the pair production process. The single-strip energy resolution of the tagging system is shown in fig.4 for 80, 60 and 40 MeV end-point photon energies.

The acquisition trigger generating the ADC gate was formed by the coincidence between the scintillation counter backing the entire microstrip tagging system and the module itself. The discrimination threshold on the calorimeter output was kept at two photoelectrons to avoid distortion of the distribution of visible energy due to detector inefficiency. The discrimination threshold used corresponds to cutting the distribution of visible energy at $-2.9\,\sigma$, for the lowest photon energy studied.

4.1 Head-on calibration and energy resolution

All the measurements in head-on geometry were carried out with the photon entering the detector face opposite to the lightguide in a $\sim$ 2.5-mm diameter beam spot with divergence less than $\pm$ 0.02° and with an angle θ, between the photon momentum and the fibers in the plane of lead foils, of $\sim$ 2°. The precision on this angle over many positionings was $\pm$ 0.5°.

Typical distributions of the visible energy deposited in the calorimeter, after selecting one tagging microstrip, are shown in fig.5. All the distributions are characterised by a high-energy tail and cannot be fitted properly by a Gaussian function alone. Instead, as shown in fig.5, each single-strip-tagged energy distribution is well fitted by a Gaussian function with a right-handed exponential tail:

$$S(x) = \begin{cases} A \exp -\frac{1}{2}(\frac{x-\mu}{\sigma})^2 & \forall x < x_j \\ A \exp -\frac{1}{2}(\frac{x_j-\mu}{\sigma})^2 \exp(\frac{x_j-x}{b}) & \forall x \geq x_j \end{cases}$$

where A, μ, σ, b and x_j (the joint point of the exponential tail to the Gaussian function) are free parameters. Table 2 shows the parameters characterizing the experimental energy distributions and their fits to a pure Gaussian and the $S(x)$ functions: mean ($< x >$) and rms for the experimental distributions and for the $S(x)$ function; μ, σ for the Gaussian fit; μ, σ, x_j for the $S(x)$ fit.

The quantity

$$\frac{A_{tail}}{A_{tot}} \equiv \frac{\int_{x_j}^{+\infty} S(x)dx}{\int_{0}^{+\infty} S(x)dx},$$

which is sensitive to the high-energy tail contributions, is also listed in tab.2. The relative significance of such a tail increases at low energies, reaching 30% at 20 MeV. Over 40 MeV, the mean ($< x >$) and the most probable value (μ) of the visible energy distributions are equal at the $\pm 2\%$ level; while at 20 MeV, they differ by about 15%. In the following, the most probable energy deposited μ will be used to characterize linearity. For evaluating the relative energy resolution σ/E, we use the ratio of σ to the most probable value μ. Due to the fact that in all best fits to our distributions $x_j > \sigma$, the resolution is equivalent to that obtained by using fwhm/2.36.

In this geometrical configuration, the light yield is 2.50 ± 0.07 photoelectrons per MeV of incident energy for module B, including all losses and inefficiencies, light attenuation and light transport. Module A gives a light yield $\sim$ 10% lower than module B, in agreement with the cosmic muon light yield. Only the measurements on module B are reported when describing linearity (fig.6), while energy resolution is studied using data from both modules.

The energy resolution is measured by selecting the photon momentum within one microstrip ($\pm 0.3\ MeV$), as long as the entries are statistically sufficient; otherwise, up to four microstrips. Figure 7 shows the energy resolution vs the incident energy, where the beam momentum resolution of the tagging system was subtracted to data in quadrature.

4.2 Head-on transversal scan

Using the photon beam with the end-point energy set at 75 MeV, the entrance face of the module was transversally scanned with a 1.8-mm beam spot and a 2^o angle of incidence to study the lateral distribution of the shower. Figure 8 shows typical energy distributions at increasing distance of the beam spot from the center of the module entrance face, while fig.9 shows the most probable energy deposited and the energy resolution.

4.3 Side-on calibration and resolution

Modules A and B were also studied in side-on configuration, i.e., with the photon hitting the center of the module and normal to the fiber axis. The hit module face was parallel to the lead foils (i.e., the photon momentum vector crosses all the Pb plates), as in cosmic ray studies. The error on the angle of incidence was $\pm 0.5^o$. Since the thickness of one module was only 9.8 cm, corresponding to a 21% leakage at 40 MeV (see §6), two modules were placed one after the other (B front A back), to contain the shower. The 10% difference in the total length compared to the head-on geometry is not relevant, since the energy leakage increases from 3.2% to 4.1% at 40 MeV.

The signals from the two modules were normalized using the most-probable visible energy deposited by cosmic muons, and added together. In the energy range studied, the rms-minimization method was also used giving weighing constants equal to the ratio of cosmic muon constants [21]. The distribution of visible energy, i.e., the

two signals summed, is shown in fig.10. In contrast to the head-on geometry, the distributions are well symmetric. Since the cosmic muon scan has shown that the two modules have the same light yield, this distribution can be linearly transformed to photoelectron scale. The photoelectron scale of module B, which collects 79% of the total energy deposited, is chosen as the absolute scale. The 10% difference between light yield of module A with respect of B introduces a systematic bias of $\sim$ -2%. Table 3 shows the parameters characterizing the experimental distributions and their fits to a pure Gaussian function.

Both photoelectron absolute yield and linearity in side-on geometry are compared with the yield and linearity obtained with prototype B in head-on geometry (fig.6b). The light yield for the two-module system is 2.70 ± 0.09 pe per MeV of incident photon energy, i.e., 8% higher than the head-on yield. A correction of $\sim$ 2% should be added to it, taking into account the systematic bias introduced by lower light yield of module A. Finally considering the energy leakage in the two configurations, the estimated difference in light yield for equally thick detectors is about 11%.

The side-on energy resolution which is significantly better than the head-on results is shown in fig.7.

4.4 Side-on lateral scanning

A 40-MeV photon beam was used to scan the modules laterally in side-on geometry. The dependence of the energy seen in the front module (fig.3c) vs the distance of the photon beam from the readout face shows the same attenuation curve as found for cosmic muons.

5 Simulation

The detector response to em showers was fully simulated making use of the GEANT code [22, 23] in the 15-120 MeV energy range, following secondary photons, electrons and δ rays down to a 10-KeV kinetic energy cutoff. At these very low energies, a cutoff might substantially affect the correctness of predictions. Therefore, the sensitivity of Montecarlo results to kinetic energy cutoff was quantified by studying the dependance of the energy resolution and sampling fraction. At a given photon energy, both the energy sampled by the fibers and the energy spread increase for decreasing cutoff values (fig.11a and 11b). However, they show similar gradients, thus the relative energy resolution (11c) does not depend on the chosen cutoff. With the 10-KeV cutoff used in the simulation, the visible energy will be underestimated by about 5% for photon energies above 30 MeV:

$$\left.\frac{E_{vis}(10KeV)}{E_{vis}(0KeV)}\right|_{E_\gamma > 30MeV} \simeq 95\%.$$

At 20 MeV, the underestimation reaches $\sim$ 10%:

$$\left.\frac{E_{vis}(10KeV)}{E_{vis}(0KeV)}\right|_{E_\gamma=20MeV} \simeq 90\%.$$

While comparing experimental data with simulation, due corrections obtained by extrapolating the results shown in fig.11 to 0-KeV cutoff were introduced.

In the side-on configuration described in §4.3 (two modules placed adjacently), 40-MeV simulated photons deposit 79.1% of primary energy in Pb-Sb alloy, 0.8% in cladding, 4.9% in glue, and 11.1% in scintillating fiber core and the longitudinal leakage is 4.1%. In the head-on configuration the energy deposited in fiber core is 10.1% while the leakage is 3.2%.

The effect of light attenuation along the fiber was taken into account in the simulation by folding the deposited energy of each shower secondary with the attenuation curve measured by the cosmic ray scan (fig.3a), to transport the deposited energy to the readout face. Although, in our energy range, light attenuation does not affect the energy resolution, it is taken into consideration for comparing the transported energy distributions and the light yields of head-on and side-on geometries.

Even though the simulation can estimate the expected photoelectron yield, provided that both the scintillating fiber quality and the optical read-out efficiency are known, an experimental normalization to the photoelectron scale is used. Such an absolute scale is set by requiring that the most probable value of transported energy distribution for 40-MeV simulated photons in head-on configuration correspond to the experimentally measured value of (101 ± 1) photoelectrons. Once this scale is set, the photoelectron statistics is introduced in the simulation by convoluting the visible energy with a Poissonian distribution. The photoelectron statistics in our detector contributes to the energy resolution with a $2\%/\sqrt{E[GeV]}$ term.

Photostatistics was also taken into account to correctly simulate the effect of discrimination threshold, due to the calorimeter being in the acquisition trigger logic. To do so, the inefficiency caused by the threshold (fig.12) was introduced in simulation. In our setup, this threshold is responsible for a $< 0.2\%$ inefficiency at 20 MeV, which has no practical effect on the measurements.

5.1 Comparing simulation with experimental data

The shower simulation described in the previous section is able to correctly reproduce the experimental distributions of the visible energy, both for side-on (fig.13a) and head-on (fig.13b) geometry. Lateral and longitudinal distributions for the energy deposited in fibers for 40-MeV photon showers in the side-on geometry are shown in fig.14. The lateral shower profile is also compared to the experimental head-on scan (fig.9), showing good agreement. A 90% fraction of the shower energy is deposited within a 2.9-cm-radius cylinder.

5.2 Linearity

To compare the simulation and experimental data, the fitting procedures described in §4.1 and §4.3 were applied to the Montecarlo data to extract the most probable values and widths of the distributions of visible energy. The experimental and the simulated linearities are compared in fig.6. The photoelectron yields in head-on and side-on geometry differ as predicted by the simulation. The difference is originated essentially by the higher sampling fraction in side-on geometry and to the different merit function due to the attenuation length in the fibers.

5.3 Sampling fraction and e/mip ratio

To determine experimentally the sampling fraction, i.e.; the fraction of incident photon energy that becomes visible, we use the photon and cosmic ray data, both in side-on geometry.

The energy released in the fiber core by 450-MeV/c muons crossing the detector was simulated with GEANT for side-on geometry. While crossing a 10 cm thick detector, 43.4 MeV are deposited in Pb-Sb alloy, 3.6 MeV in glue, 0.7 MeV in cladding, and 9.2 MeV (16.2 % of total) in core.

The light yield for a muon is 23.0 photoelectrons per cm of crossed detector, while depositing 0.92 MeV in fiber core. Therefore, 25.0 photoelectrons are seen for each MeV of energy deposited in fiber core. As 2.7 photoelectrons are seen for each MeV of incident photon energy, the photon sampling fraction of the detector studied is:

$$f_\gamma^{experimental} = \frac{2.70\ pe/MeV}{25\ pe/MeV} = 10.8 \pm 0.4\ \%$$

to be compared with 11.1% predicted by the simulation. The agreement is good, considering that the simulation does not reproduce the cosmic muon momentum distribution as selected in the experimental setup using the Pb filter in the counter telescope. Moreover, both em and muon sampling fractions could be higher than quoted, due to the fact that the simulation does not consider the effect of the Čerenkov light generated in cladding and glue. Part of this light travels to the core, where it is wave-length shifted and trapped.

To compare the em response of calorimeters constructed with different techniques, it is customary [24] to express the absolute measurement of the sampling fraction for em showers in terms of the ratio (e/mip ratio) between the signals released by em showers, to those released by mip's depositing the same energy in the calorimeter. For fully contained showers, the simulated photon sampling fraction in the side-on geometry f_γ is 11.5%, whereas the sampling fraction for minimum ionizing muons f_μ is 16.2%, giving an e/mip ratio:

$$e/mip = f_\gamma / f_\mu = 0.71$$

5.4 · Energy resolution

One of the aspects to be explained by simulation is the asymmetric shape characterizing the head-on data which is well reproduced by simulation.

The 2° incidence angle of the photon beam guarantees that complete channeling of photons in the fibers (which, however, would originate a low-energy tail similar to that of shower noncontainment) does not play an important role. The observed asymmetry appears, instead, to be related to path-length fluctuations associated with the channeling of shower secondaries. The angular distribution of the shower secondaries with respect to the parent photon is expected to be very spread out at the energies considered, following the $\cos^2\theta$ dependence according to multiple scattering considerations[25],[26]. However, in the very early stages of shower development, a small fraction of secondaries still remembers the parent direction. For photons entering the detector at a very low angle with respect to the fiber axis, first-generation electrons can travel long distances inside the fiber. This is confirmed by simulation. In fig.15 the distributions of path-lengths in the fiber core are shown for 40-MeV photons, at various incidence angles (from $\theta = 2°$ to $\theta = 90°$). The Landau tails in the energy deposition of charged secondaries were turned off in the simulation, with no difference being found. The long path-length samplings causing the 'secondary channeling' give rise to high-energy tails in the visible energy distributions. These tails become less and less significant as the angle θ increases. On the other hand, the path-length distributions for 20-MeV and 120-MeV photons in the head-on configuration are found to be the same, suggesting that, for the energy range under consideration, the path-length distribution is determined only by geometrical incidence. However, with the increasing photon energy, the number of fiber crossings increases and the high energy tails in the visible energy distribution become less significant.

Although the fitting function used to extract the energy resolution in the head-on data is relatively tail-insensitive, we still find that the side-on resolution is better. When the angle θ between the parent photon and the fiber axis increases, the average path length decreases; but, since the number of fiber crossings increases(fig.16c), the energy resolution improves (fig.16a), reaching an asymptotic value above 30 degrees.

Experimental data at $\theta = 6°$ supports this interpretation as the trend shown by energy resolution and light yield by comparing (tab.4) and (tab.2) is in agreement with simulation. Furthermore, at $\theta = 6°$ the high energy tails are still present as predicted by simulation.

5.5 Energy scaling

The energy resolution $\sigma/\sqrt{E[GeV]}$ for the studied modules for both head-on and side-on geometries is shown in fig.17 as a function of the photon energy, along with the predictions from simulation. The side-on resolution scales with $E^{-\frac{1}{2}}$, while the head-on resolution exhibits a nonscaling term, linearly added. Table 5 shows the fit results of the energy resolutions for side-on and head-on geometries.

6 Summary and Conclusions

We have studied two Pb/SCIFI em calorimeters characterized by a 35:50 ratio by volume and have tested them with a tagged photon beam in the $20 - 80\,MeV$ energy region.

In good geometrical conditions (large angle between the photon direction and the fiber axis), the fraction of sampled energy for an em shower is 11.1%. The visible-energy distribution is Gaussian and the energy resolution scales as $E^{-\frac{1}{2}}$.

In critical geometrical conditions (i.e., with the photon travelling almost parallel to the fiber axis), the visible-energy distribution is not symmetric, with a tail towards high-energy deposits. The energy resolution, even using tail-insensitive estimators (as mentioned in §4.1), is worse than the resolution in good geometrical conditions and does not scale as $E^{-\frac{1}{2}}$.

The detector resolution is parametrized as:

$$\frac{\sigma}{E} = \frac{\alpha}{\sqrt{E[GeV]}} + \beta(\theta, E)$$

where in the $20 - 80\,MeV$ energy range:

$$\beta(2^\circ, E) \sim constant$$

$$\beta(\theta \geq 30^\circ, E) = 0.$$

The scaling term α of the energy resolution found in side-on geometry agrees, within the errors, with the scaling term found in head-on geometry. It includes a 2% term in quadrature, originated by the readout photostatistics.

In side-on geometry with optimized conditions of light collection, an $\alpha = 4.5\%$ is expected, while for total shower containment a scaling term as good as 4.0% can be reached.

The experimental and simulation data described here demonstrate that the Pb/SCIFI technique constitutes an economical, mechanically simple solution for em calorimetry at very low energy, characterized by good efficiency, linearity and energy resolution.

An experimental investigation of the prototypes with photon energies of the order of 1 GeV is being planed to be carried out at the Frascati tagged photon beam of JET TARGET facility [27].

7 Acknowledgements

We should like to thank E. Cima, M. Iannarelli, G. Nobili, and E. Turri for their technical help in running the beam test. Special thanks are due to R. Baldini and to the Fenice group, who helped in many ways, as well as to F.Anulli for his help in early stages of the tests. Fruitful discussions with S. Bertolucci, S.Miscetti and C. Schaerf are also kindly acknowledged. Finally, we are in debt to F.Bertino and D.Riondino

for the CAD processing of the technical drawings and L.Invidia for technical editing. This research was supported in part by the Italian INFN Gruppo V and the US National Science Foundation (contract NSF PHY 89-21146).

References

[1] D.W. Hertzog et al., *Nucl. Instr. and Meth.* **A294**, (1990) 446-459.

[2] K. Beard et al., CEBAF report CLAS-NOTE 90-013 (25 Oct., 1990).

[3] H. Blumenfeld et al., *Nucl. Instr. and Meth.* **A235**, (1985) 326-331.

[4] for a review of early experimentation see P. Sonderegger, *Nucl. Instr. and Meth.* **A257**, (1987) 523-527.

[5] D.W. Hertzog et al., Int. Conf. on Calorimetry in High Energy Physics, 29-Oct. to 1-Nov.,1990, Fermilab, Batavia, USA, eds. D.F. Anderson, M. Derrick, H.E. Fisk, A. Para and C.M. Sazama (World Scientific) p. 135, also a University of Illinois(U-C) report (NPL)-91-002 (1991).

[6] A.Antonelli et al., KLOE proposal, Frascati report LNF-92/019(R)(1992).

[7] Proposal for a ϕ-factory, LNF note LNF90/031(R), 1990.

[8] Action Tool and Die Co., 3374 Precision Dr., Rockford, IL 61109 (U.S.A.). The grooved foils were produced by custom rolling 0,46-mm-thick flat lead plates.

[9] Optectron, Z.A. Courtaboeuf, BP 535, Av. du Québec, F-91946 Les Ulis, France.

[10] Bicron, Inc., 12345 Kinsman Rd, Newbury (OH) 44065-9677 USA. The BC600 optical cement has a 1.56 refraction index (B.Richards, Bicron, Inc., private communication).

[11] Nuclear Enterprise. Sighthill Edinburgh EH11 4BY Scotland.

[12] Pol.Hi.Tech, Carsoli (AQ) Italy.

[13] Review of Particle Properties, Phys. Rev. **D45**(1992)III.15

[14] THORN EMI Electron Tubes Limited Bury Street Ruislip Middlesex HA4 7TA England.

[15] W.T. Welford and R. Winston, **The optics of nonimaging concentrators**, Academic Press (New York) 1978.

[16] We used 11-bit, LRS 2249W analog-to-digital converters manufactured by LeCroy Research Inc., 700 South street Spring Valley, New York 10977, U.S.A.

[17] L.S. Peak and P. Soler *Nucl. Instr. and Meth.* **A301**, (1991) 341-349. We used typically $N_{pe} = 100 - 200$.

[18] S. Bianco et al, *Nucl. Instr. and Meth.* **A315**, (1992) 322-326.

[19] S. Bianco et al., in preparation. The new production of Pol.Hi.Tech 0042 fibers in 1992 has shown a much improved scintillation efficiency.

[20] D. Babusci et al.,*Nucl. Instr. and Meth.* **A305**, (1991) 19-24.

[21] S. Bianco et al., KLOE note/33-92 (1992, unpublished).

[22] R. Brun et al., GEANT Reference Manual, CERN DD/EE/84-1, V3.14.

[23] S. Bianco et al., KLOE note/24-92 (1992, unpublished).

[24] C. Fabjan, *Techniques and Concepts of High Energy Physics - III*, T.Ferbel, ed. (Plenum Pub. Corp., 1985).

[25] H.G. Fisher, *Nucl. Instr. and Meth.* **156**, (1978) 81.

[26] H. Lengeler, W. Tejessy and M. Deutschmann, *Z. Physik* **175** (1963) 283.

[27] N. Bianchi et al., *Nucl. Instr. and Meth.* **A317**, (1992) 434-444.

Table 1: Significant optical parameters of the fibers utilized.

	n_{core}	n_{clad}
Pol.Hi.Tech 0042(90)	1.590	1.492
Optectron S101-S	1.592	1.416

Table 2: Significant experimental and fit parameters for head-on geometry. The energy deposited is given in photoelectron units. The tail-joint parameter x_j is given in σ units.

$E_\gamma[MeV]$		data	gauss fit	$S(x)$ fit
	$< x >$	70±1		69
	$rms(\%)$	45.0		43.4
	μ		66±1	53±1
22	$\sigma/\mu(\%)$		42±2	33±2
	x_j			-1.0±0.2
	$\chi^2/d.o.f.$		2.4	1.1
	$A_{tail}/A_{tot}(\%)$			29±9
	$< x >$	103±1		103
	$rms(\%)$	29.3		28.5
	μ		102±1	101±1
40	$\sigma/\mu(\%)$		27.2±0.5	26.1±0.6
	x_j			-1.2±0.3
	$\chi^2/d.o.f.$		1.6	1.2
	$A_{tail}/A_{tot}(\%)$			14±7
	$< x >$	153±1		154
	$rms(\%)$	25.3		24.4
	μ		152±1	149±1
59	$\sigma/\mu(\%)$		23.9±0.4	22.0±0.6
	x_j			-1.2±0.2
	$\chi^2/d.o.f.$		1.5	1.2
	$A_{tail}/A_{tot}(\%)$			16±4
	$< x >$	188±1		190
	$rms(\%)$	26.5		24.4
	μ		189±1	188±1
75	$\sigma/\mu(\%)$		22.8±0.5	21.2±0.7
	x_j			-1.5±0.3
	$\chi^2/d.o.f.$		1.1	0.8
	$A_{tail}/A_{tot}(\%)$			9±5

Table 3: Significant experimental and fit parameters for side-on geometry. The energy deposited is given in photoelectron units.

$E_\gamma[MeV]$		data	gauss fit
50	$< x >$	134±1	
	$RMS(\%)$	25.5	
	μ		135±1
	$\sigma/\mu(\%)$		22.6±0.9
	$\chi^2/d.o.f.$		1.04
60	$< x >$	161±1	
	$RMS(\%)$	21.2	
	μ		162±1
	$\sigma/\mu(\%)$		19.6±0.9
	$\chi^2/d.o.f.$		0.7
75	$< x >$	204±1	
	$RMS(\%)$	18.2	
	μ		204±1
	$\sigma/\mu(\%)$		17.6±0.3
	$\chi^2/d.o.f.$		0.8

Table 4: Significant experimental parameters and fit parameters for 6° incidence. The deposited energy is given in photoelectron units. The tail-joint parameter x_j is given in σ units.

$E_\gamma[MeV]$		data	gauss fit	$S(x)$ fit
60	$< x >$	153±1		152
	$RMS(\%)$	25.1		24.1
	μ		151±1	150±2
	$\sigma/\mu(\%)$		23.3±0.8	21.5±0.9
	x_j			-1.1±0.5
	$\chi^2/d.o.f.$		1.3	0.95
	$A_{tail}/A_{tot}(\%)$			18±5
74	$< x >$	190±1		199
	$RMS(\%)$	22.7		21.7
	μ		190±1	187±1
	$\sigma/\mu(\%)$		21.1±0.5	20.5±0.6
	x_j			-1.2±0.1
	$\chi^2/d.o.f.$		1.1	.99
	$A_{tail}/A_{tot}(\%)$			14±4

Table 5: Relative energy resolution (σ/E) measured and simulated, both for side-on and head-on geometries.

	experiment	simulation
side-on	$(4.81 \pm 0.06)\%\ E^{-\frac{1}{2}}$	$(4.70 \pm 0.05)\%\ E^{-\frac{1}{2}}$
head-on	$(4.7 \pm 0.1)\%\ E^{-\frac{1}{2}} + (3.4 \pm 0.6)\%$	$(4.6 \pm 0.3)\%\ E^{-\frac{1}{2}} + (3.8 \pm 1.3)\%$

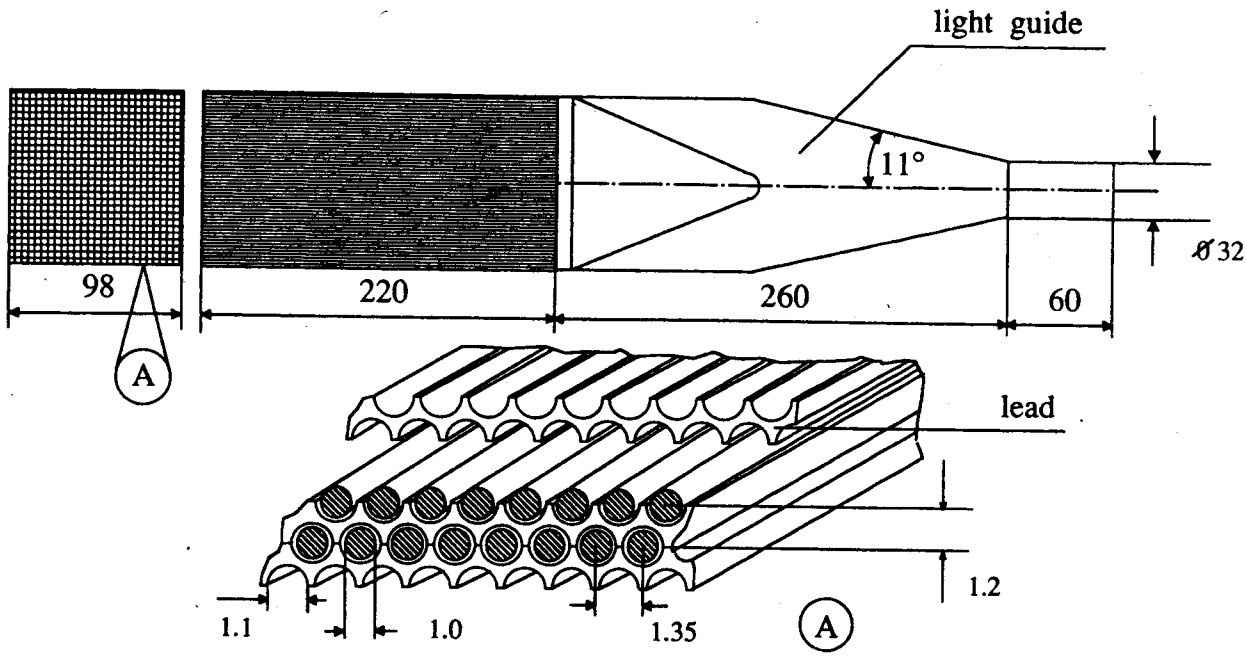

Figure 1: Assembly of grooved lead foils and scintillating fibers. All dimensions are in millimeters.

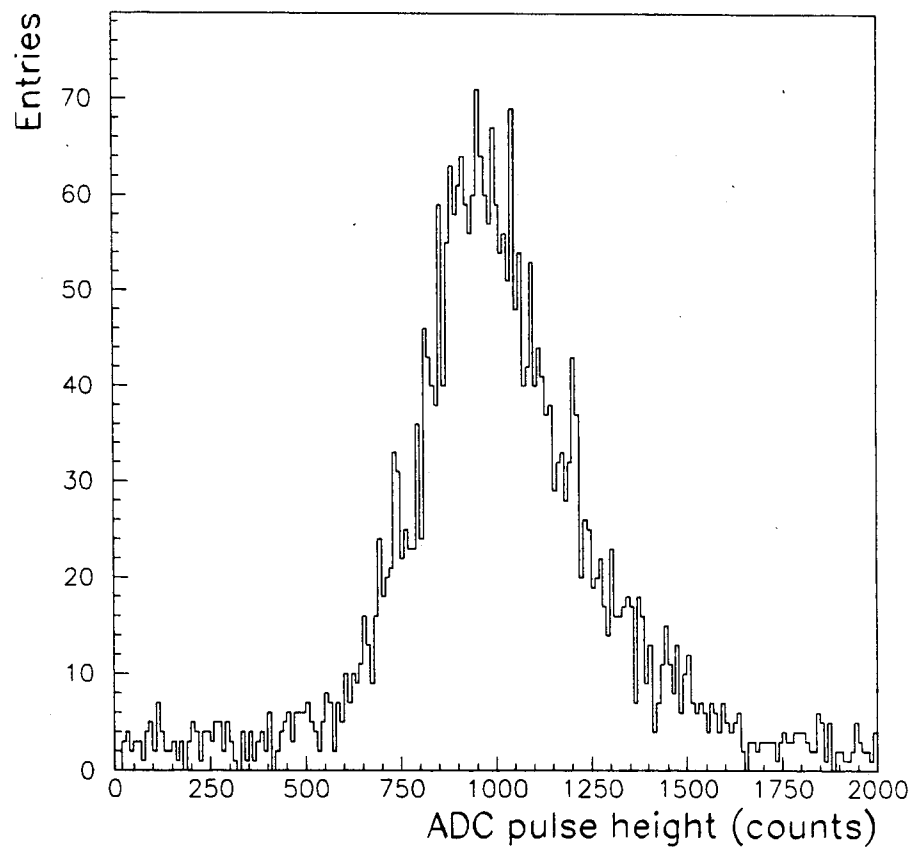

Figure 2: Distribution of visible energy for cosmic ray muons passing through one of the detector modules and 30 cm thick Pb absorber. The muons are incident on the detector face parallel to grooved Pb foils, at a distance of 10 cm from the readout face.

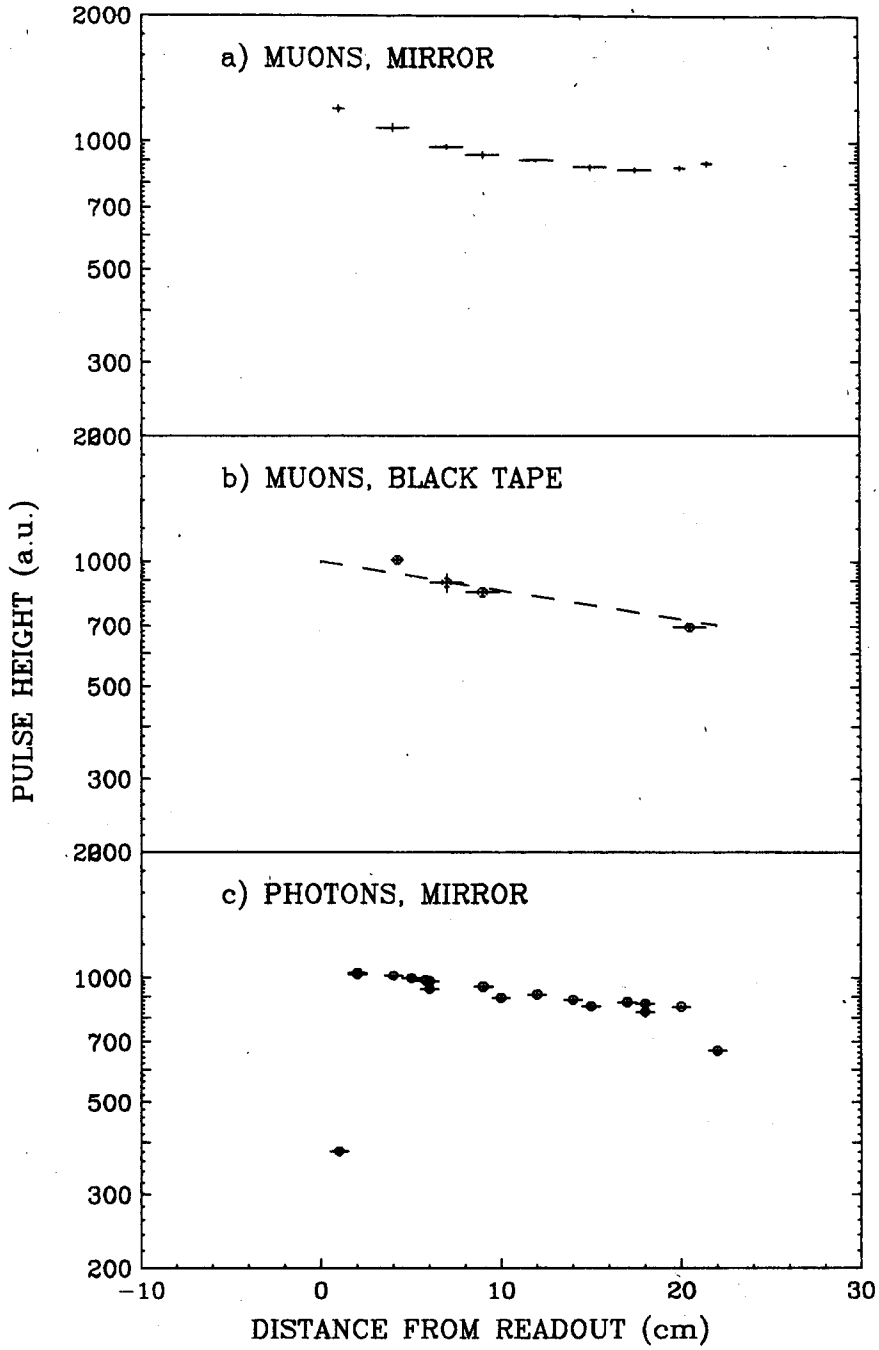

Figure 3: Attenuation curve for the light excited by (a) cosmic mip's in modules with aluminized face; (b) cosmic mip's in modules with face covered by black tape, and the attenuation curve (dashed) for fibers before assembly in the Pb matrix; (c) 40-MeV photons in modules with aluminized face.

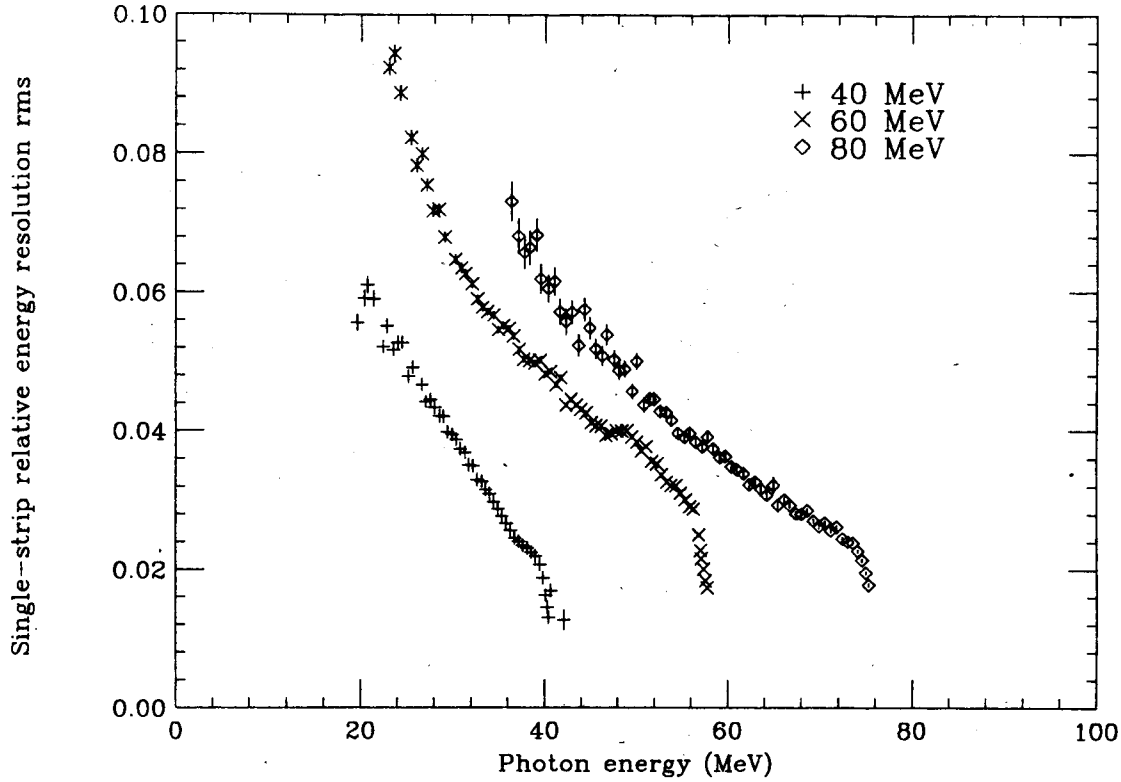

Figure 4: Single-strip energy resolution of the LADON microstrip tagging system, for 40, 60 and 80 MeV end-point photon energies.

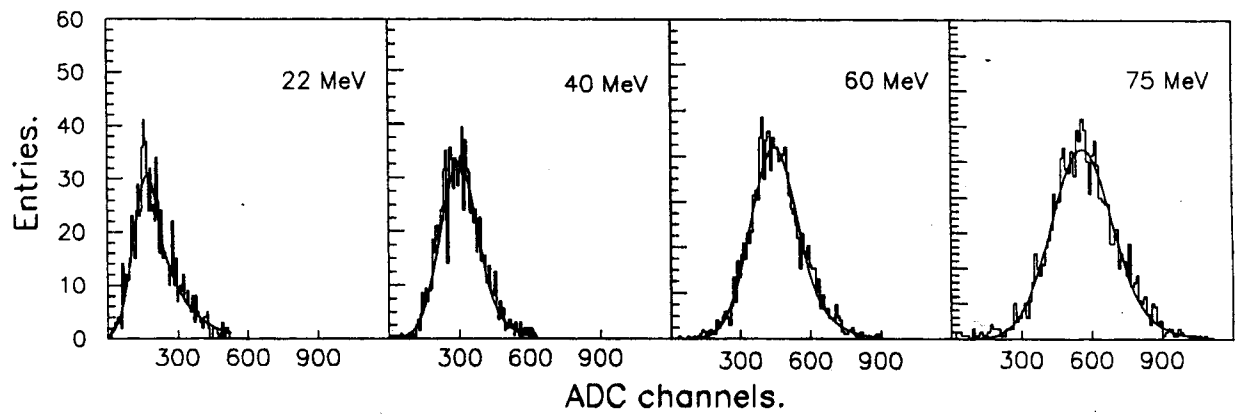

Figure 5: Experimental distribution of visible energy for photons in head-on geometry, with $S(x)$ fit superimposed.

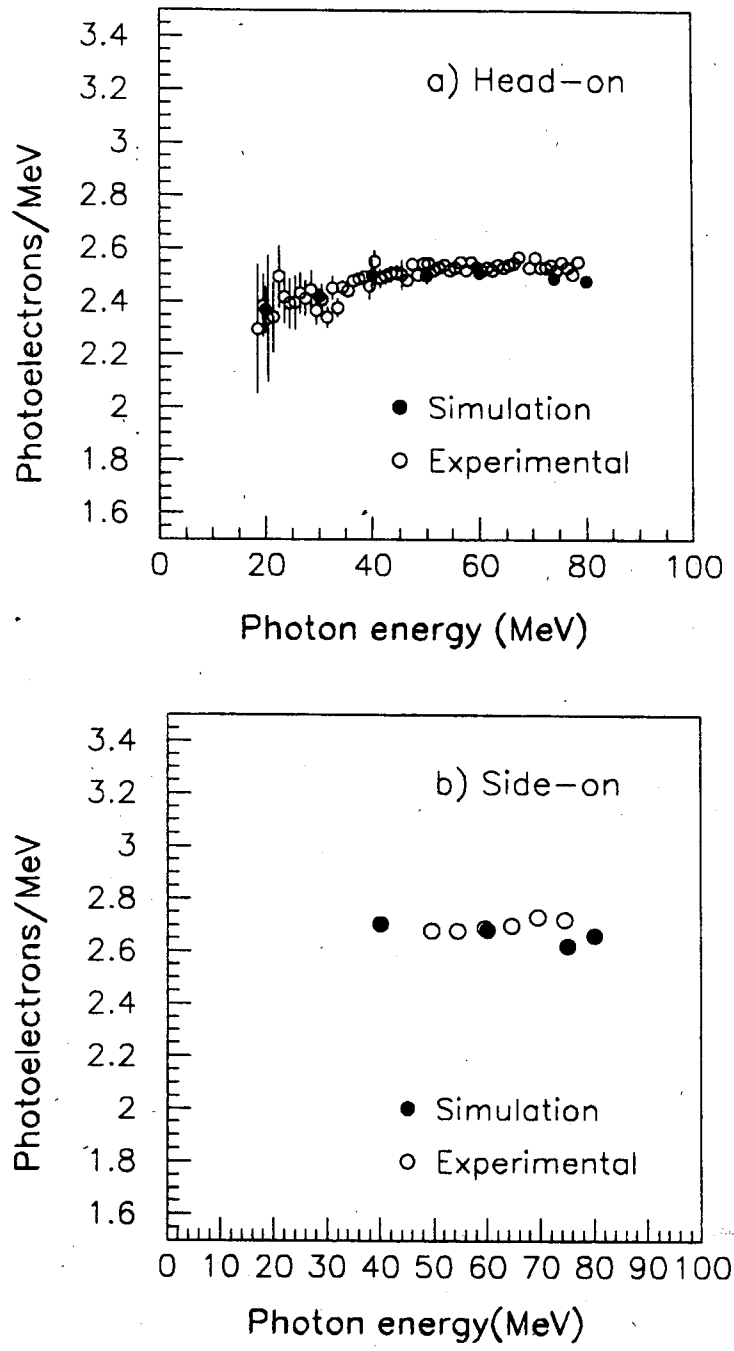

Figure 6: Linearity of the modules expressed as the ratio (photoelectrons)/(incident energy in MeV) as a function of the incident energy and the points from Montecarlo: (a) head-on geometry; (b) side-on geometry.

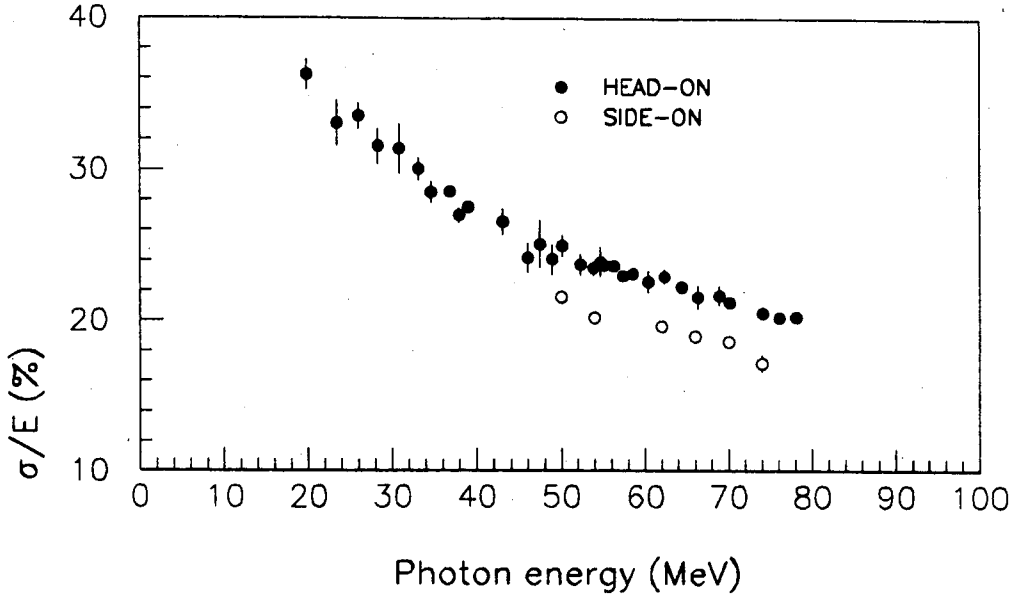

Figure 7: Head-on and side-on energy resolution of the modules tested. The vertical error bar is the statistical error of the best fits.

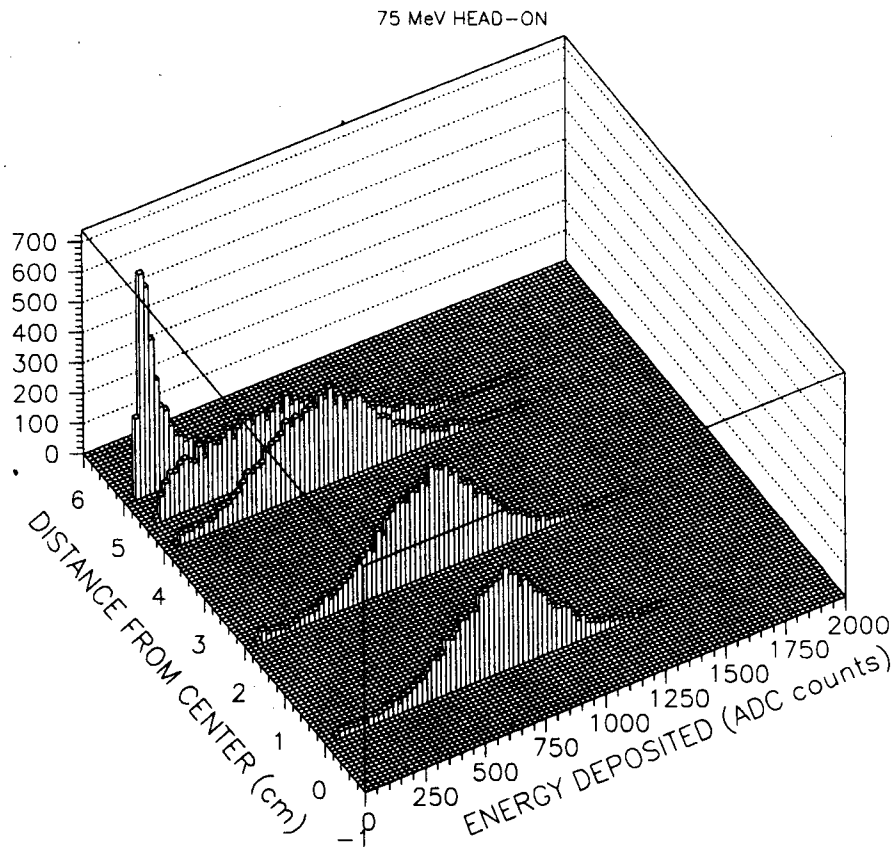

Figure 8: Changes in visible energy distribution, as the distance between beam spot and the center of the module entrance face is increased.

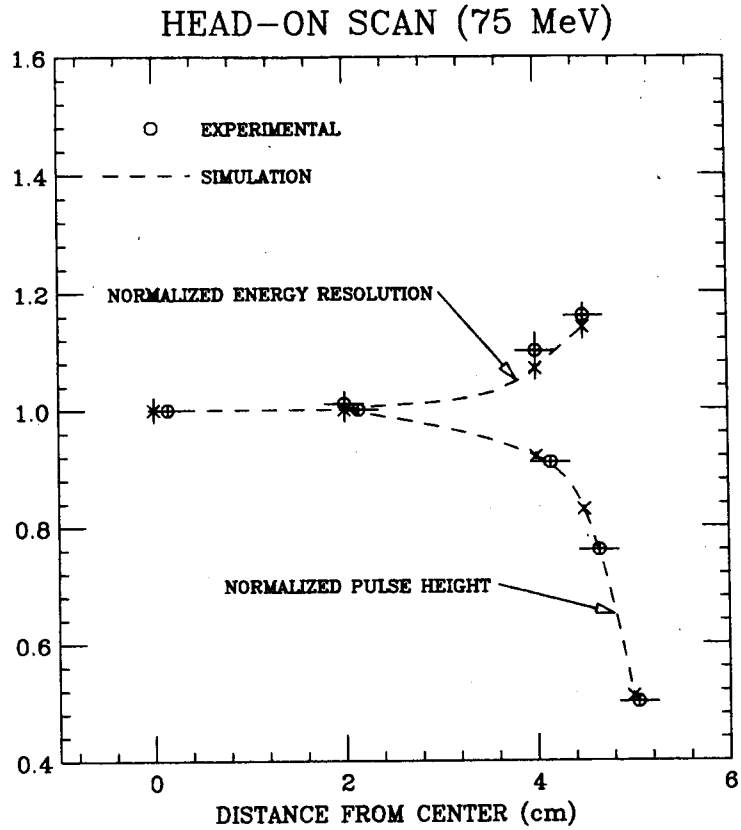

Figure 9: Relative energy resolution and most-probable ADC pulse height as a function of distance of beam spot from the centre of the module entrance face.

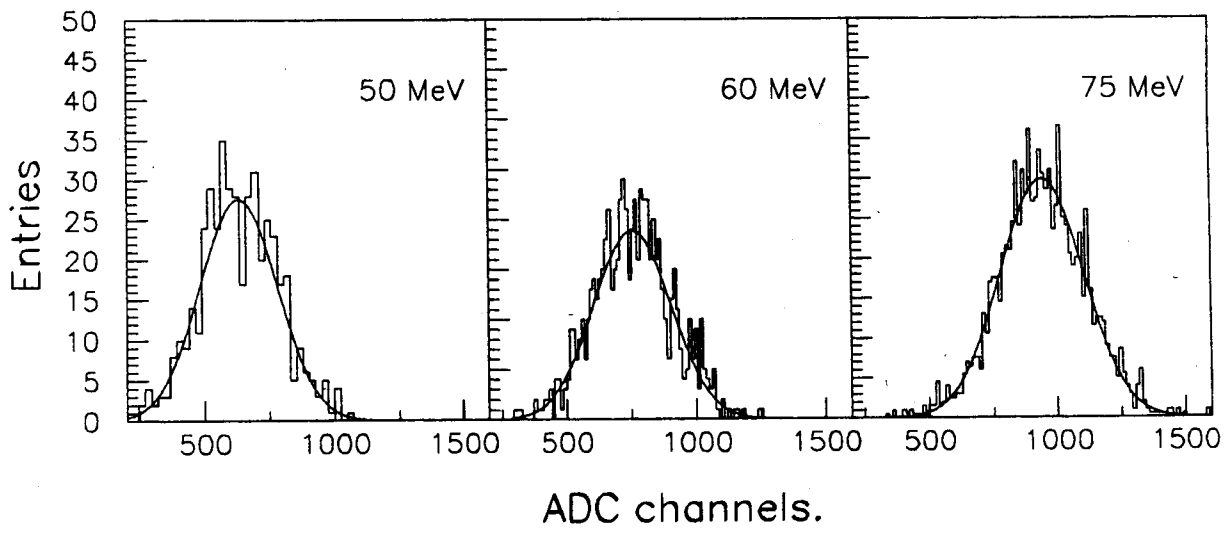

Figure 10: Experimental distribution of visible energy for photons striking side-on, with Gaussian fit superimposed.

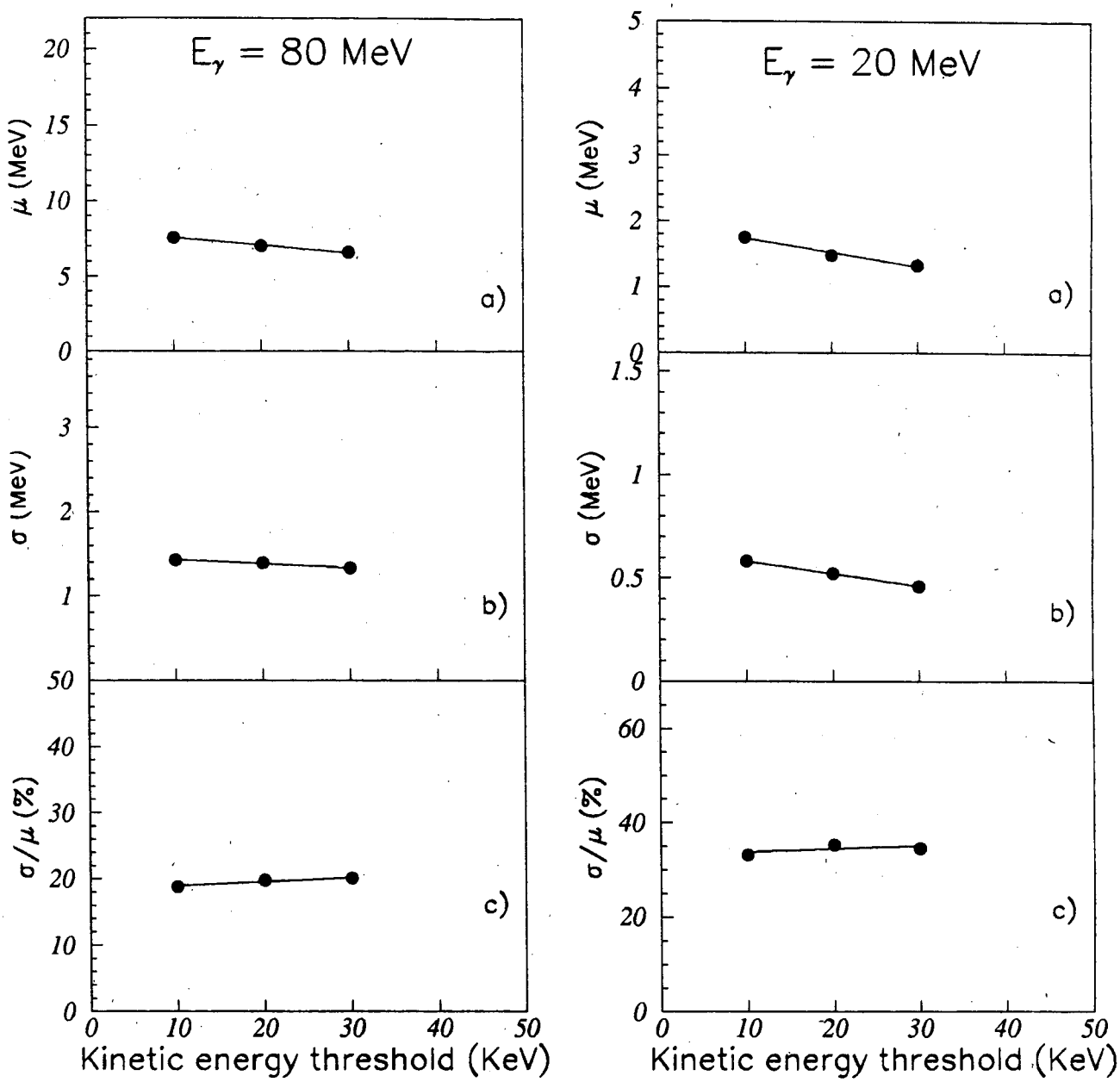

Figure 11: Dependance of Montecarlo results on the kinetic energy cutoff: (a) most probable value of visible energy; (b) σ; (c) relative energy resolution.

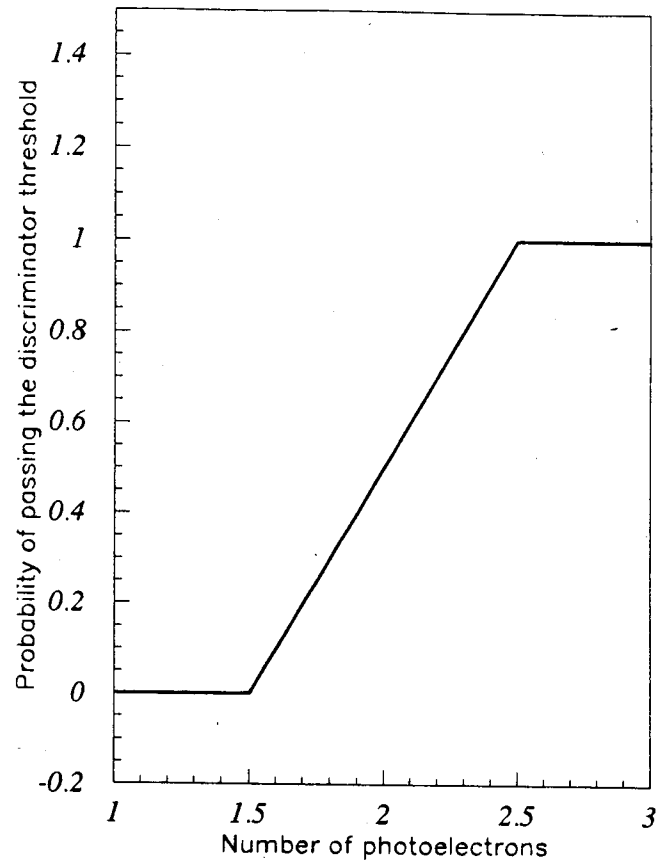

Figure 12: Discrimination threshold function introduced in the simulation.

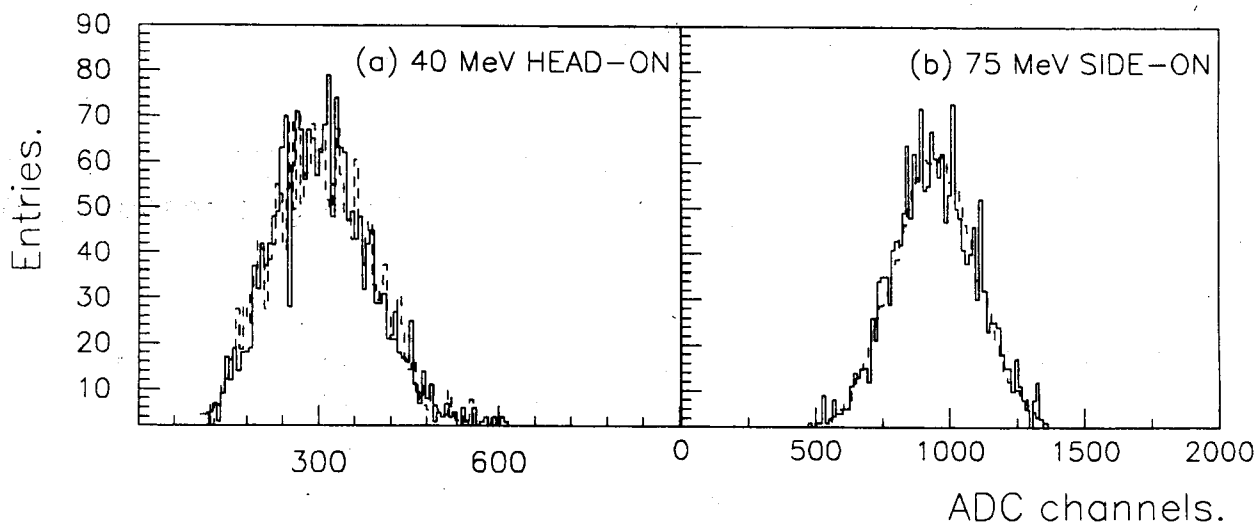

Figure 13: Comparison of simulated (continuous) and experimental (dash) distributions of visible energy for (a) head-on and (b) side-on configurations.

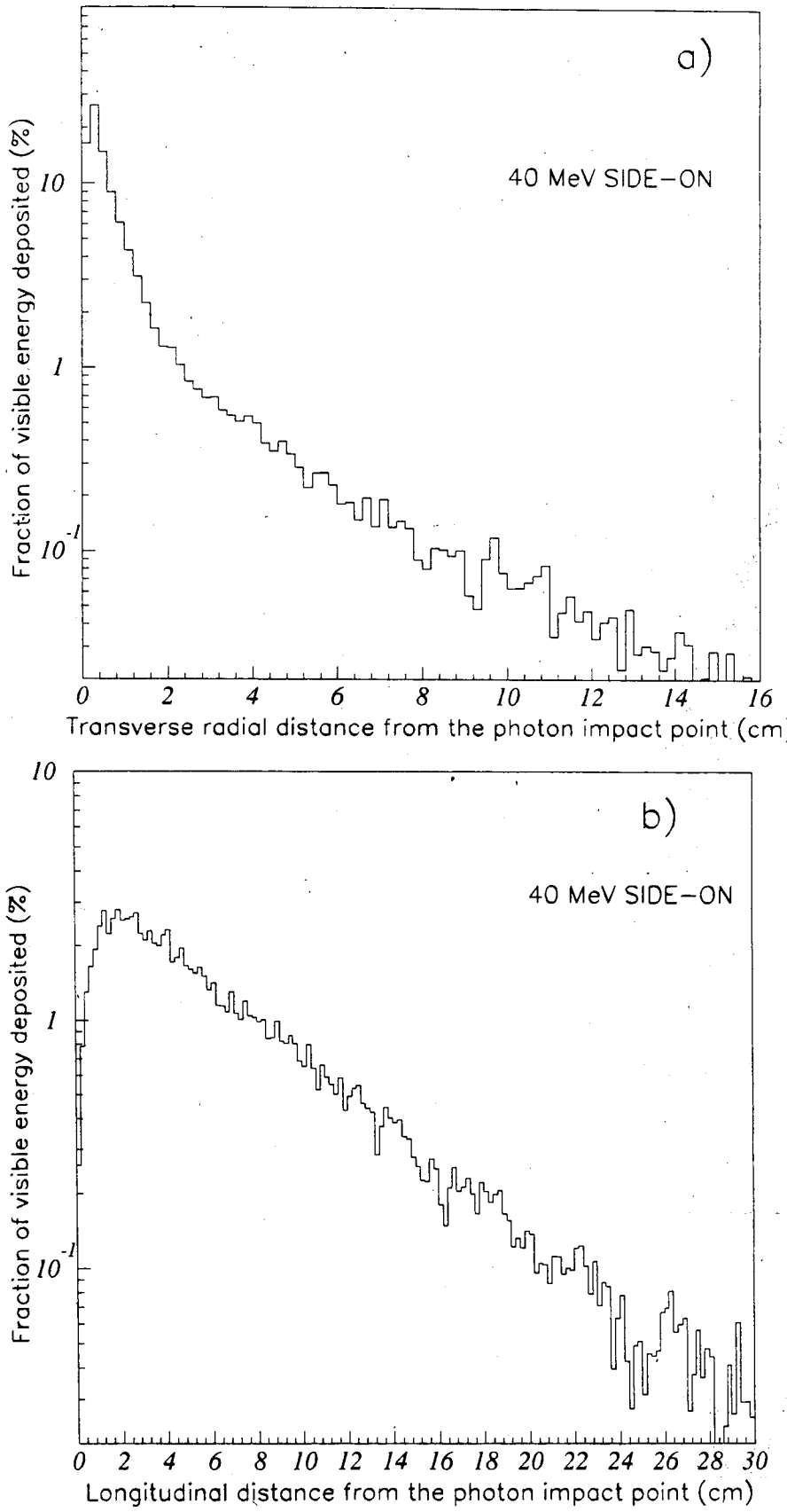

Figure 14: Simulated (a) lateral and (b) longitudinal shower profiles in side-on geometry, initiated by 40-MeV photons.

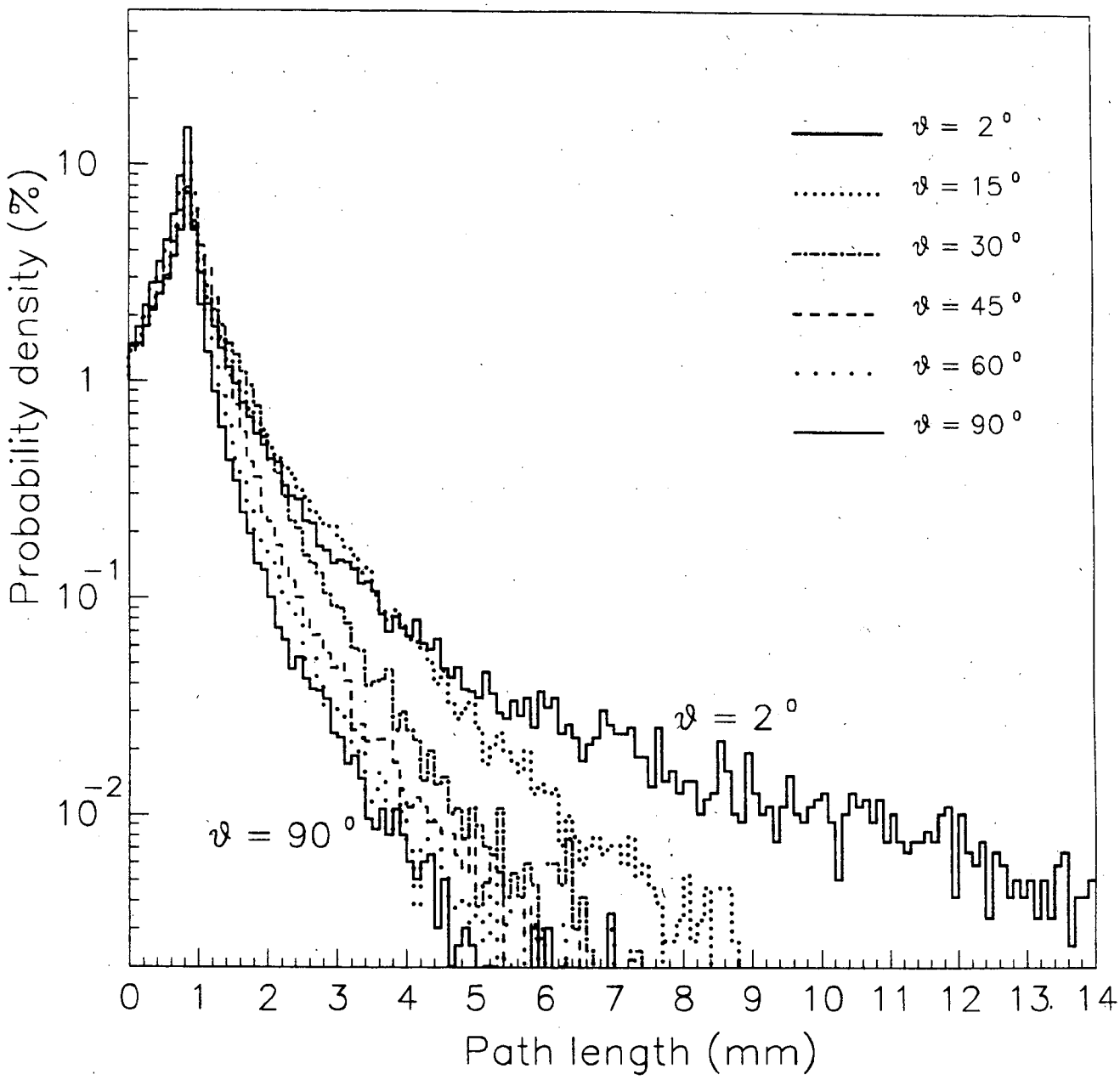

Figure 15: Distribution of path length in fiber core for simulated 40-MeV photons with various values of angle θ, between the photon momentum and the fibers in the plane of lead foils.

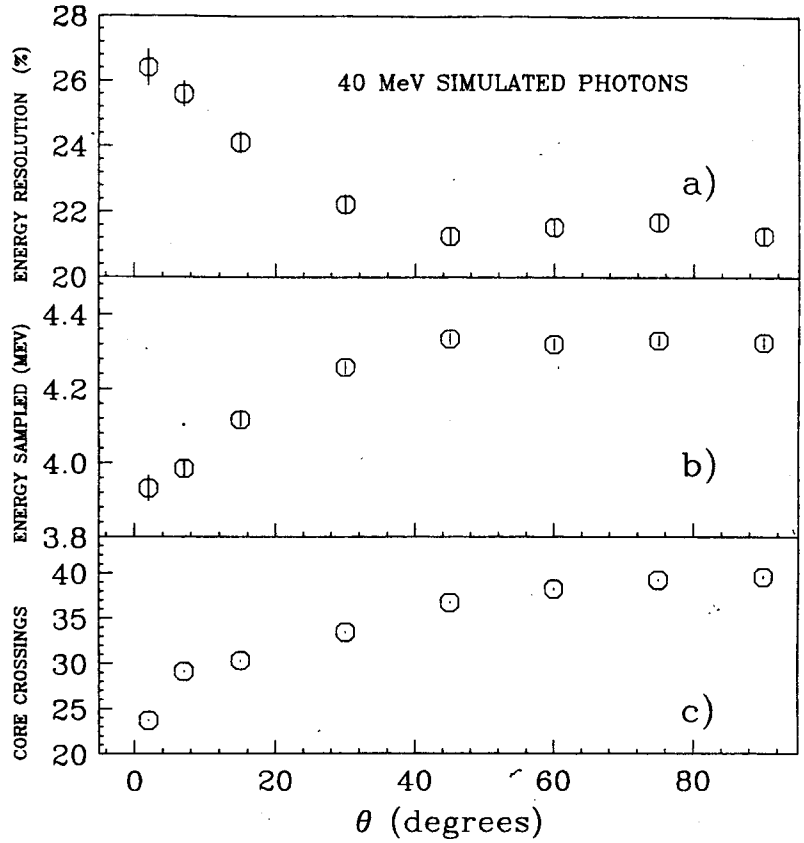

Figure 16: Dependance of em shower characteristics on the angle θ, between the photon momentum and the fibers in the plane of lead foils: (a) energy resolution; (b) sampled energy in the fiber core; (c) number of fiber crossings for charged shower-secondaries. These results are obtained by simulating 40-MeV photons in a $40 \times 40 \times 40\, cm^3$ detector and without considering the contribution due to photoelectron statistics.

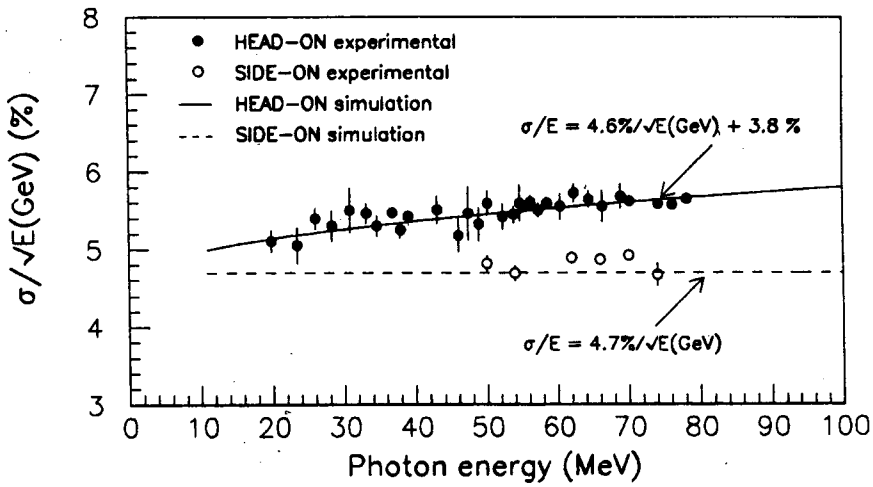

Figure 17: Relative energy resolution for the two modules tested, for head-on and side-on geometry. Also shown are the two fits obtained for the Montecarlo results.